Materials Advances

ROYAL SOCIETY OF CHEMISTRY

PAPER

View Article Online
View Journal | View Issue

Cite this: *Mater. Adv.*, 2024, 5, 6162

Exploring luminescence quenching mechanisms and temperature sensing capabilities of $LiSrYW_3O_{12}:Sm^{3+}$ phosphors

F. Ayachi, K. Saidi and M. Dammak *

Optical thermometry has emerged as a crucial non-contact method for temperature measurement, serving a broad array of applications. This technique delivers precise readings without the need for physical contact, proving especially valuable in situations where traditional contact-based methods are impractical. However, the pursuit of heightened accuracy in optical thermometry remains an ongoing pursuit. Within this context, the advancement of luminescent thermometers assumes significant importance, offering the promise of enhanced temperature sensing capabilities. Through the exploration of novel materials and innovative strategies, the goal is to elevate the precision of these sensors, paving the way for more dependable temperature measurements in various environments. Therefore, the focus of the present study lies in the synthesis of a series of $LiSrYW_3O_{12}$ (LSYW):x%Sm^{3+} phosphors using the solid-state reaction technique, where x varies from 0.03 to 0.15. The investigation delves into the structures, morphologies, UV-Visible absorption, and luminescent characteristics of these phosphors. The down-conversion luminescence properties were studied under 405 nm laser excitation, leading to the determination of the optimal doping concentration at x = 0.05. Subsequent in-depth analysis focused on the optical temperature sensing properties, employing the fluorescence intensity ratio (FIR) method. The FIR of the $^4F_{3/2}/^4G_{5/2} \rightarrow {}^6H_{7/2}$ transition consistently increased with temperature across the range of 300–583 K. The maximum relative sensitivities were determined as 1.58% K^{-1} (at 301 K). These findings underscore the exceptional potential of LSYW doped with Sm^{3+} as a highly effective material for applications in high-temperature sensing. Through this research, the pursuit of more accurate and reliable temperature measurements takes a significant step forward, offering promising avenues for further exploration and utilization.

Received 15th March 2024,
Accepted 20th June 2024

DOI: 10.1039/d4ma00276h

rsc.li/materials-advances

1. Introduction

Temperature is a significant factor in the domains of material engineering and equipment manufacture, as it often influences several physical and chemical aspects of goods to a certain degree. Thus, applications in industry are extremely interested in thermometers since they can measure an object's temperature correctly.[1–3] When measuring temperature, contact thermometers – including thermocouple thermometers are susceptible to a number of limitations. Rare earth ions, particularly the trivalent Sm^{3+}, play a significant role as activator ions in the development of novel luminescent materials.[4–6] Due to its multi-energy structure and orange-red light emissions from its $^4G_{5/2}$ level, Sm^{3+} has attracted a lot of interest recently. Meanwhile, its high quantum efficiency makes it a promising candidate for use in high-density optical storage, underwater communication, and color display.[7] Extensive theoretical and experimental investigations have been conducted on Sm^{3+} ions.[8,9] Their unique 4f–4f transitions result in red-orange emissions, making materials activated with Sm^{3+} ions desirable for various applications, including white light-emitting diodes (w-LEDs). Recent research has focused on utilizing different host materials, such as $Ba_2Ca(BO_3)_2:Sm^{3+}$, $Ba_2CaZn_2Si_6O_{17}:Sm^{3+}$, and $LiBaPO_4:Sm^{3+}$, to achieve red-orange emissions.[10–12] Additionally, the potential applications of Sm^{3+}-doped materials as red phosphors can be enhanced through codoping with other lanthanide ions.[13,14] However, Sm^{3+} doped tungstate phosphors with Li, Na, and K ions show excellent luminous intensity along with chemical and thermal stability.[15,16] Due to their combination of high thermal conductivity, excellent thermal and mechanical stability, low phonon energy (around 900 cm^{-1}), high melting point (1240 °C), and chemical stability, complex tungstate structures are considered promising host matrices for rare earth doping.[17–20]

Laboratoire de Physique Appliquée, Faculté des Sciences de Sfax, département de Physique, Université de Sfax, BP, 1171, Sfax, Tunisia.
E-mail: madidammak@yahoo.fr, Mohamed.dammak@fss.usf.tn

Binary alkaline earth tungstates, denoted as $MLn_2(WO_4)_4$ (with M representing an alkaline earth bivalent metal ion and Ln representing trivalent rare-earth ions), are categorized among scheelite-structured compounds. The extensive investigation of scheelite-structured binary molybdates and tungstates has been driven by their remarkable up-conversion (UC) photoluminescence properties, as documented in prior studies.[21,22] Specifically, binary $NaLn(WO_4)_2$ compounds, when doped with rare-earth ions, display a tetragonal phase with the I_{41}/a space group, falling under the broader classification of scheelite-type structures. This phase is frequently utilized to facilitate the partial substitution of trivalent rare-earth ions (Ln^{3+}) by Ho^{3+} and Yb^{3+} ions, introducing disorder in the tetragonal phase at the lanthanide site of Ln^{3+}.[23–25]

To date, a single report on ternary tungstates with a general composition of $NaMLn(WO_4)_3$ has been documented, where M represents Ca^{2+}, Sr^{2+} and Ba^{2+}, and Ln represents La^{3+}, Gd^{3+} and Y^{3+},with Ho^{3+}/Yb^{3+} codopage.[26,27] In this article, we will explore $LiSrYW_3O_{12}$ doped with Sm^{3+} for thermometry applications. This paper explores the synthesis of LSYW:Sm^{3+} materials through the solid-state reaction method. The down-conversion luminescence characteristics of LSYW:Sm^{3+} were assessed at room temperature using a 405 nm laser. Furthermore, the temperature dependence of LSYW doped with 5% Sm^{3+} was comprehensively investigated over the range of 301 to 583 K.

2. Experimental procedure

2.1. Synthesis

LSYW microcrystalline samples doped with Sm^{3+} ions were synthesized using a high-temperature solid-state reaction technique. The starting materials, with a high purity of 99.999%, included Li_2CO_3, $SrCO_3$, Y_2O_3, WO_3 and Sm_2O_3 (Sigma-Aldrich).

Various doping concentrations of Sm^{3+} (0.03, 0.05, 0.07, 0.1, and 0.15 relative to Y^{3+} ions) were employed. Stoichiometric amounts of the high-purity chemicals were meticulously mixed and ground using an agate mortar. Subsequently, the mixture was gradually heated to 350 °C for 16 hours to eliminate gases. The resulting powder was then compressed into cylindrical pellets and heated at 900 °C for 10 hours.

2.2. Characterization

The X-ray diffraction (XRD) patterns of the phosphors were measured in the 2θ range of 5–60° using an X-ray diffractometer (Bruker D8, Germany) equipped with Cu Kα radiation (λ = 1.5405 Å), operating at 40 kV and 30 mA for phase identification. UV-vis-NIR absorption was analyzed utilizing a UV-vis-NIR spectrometer (PerkinElmer Lambda 950). Morphological characteristics of the samples were investigated *via* scanning electron microscopy (SEM) (JEOL, JSM 6510LV). Temperature-dependent emissions were studied using a JOBIN YVON HR 320 spectrometer with a 405 nm laser excitation source. The temperature of the sample was varied from room temperature to 588 K with the interval of 10 K.

3. Results and discussions

3.1. Characterization of crystalline phase

The XRD patterns were employed to investigate the crystal structure and phase purity of the materials. Fig. 1. displays the X-ray diffraction patterns of microcrystals LSYW:$x$$Sm^{3+}$ with x = 0.03, 0.05, 0.07, 0.1, and 0.15, registered in the range of 5–65°. According to the XRD patterns of LSYW (JCPDS No. 96-154-6037), the samples exhibit a tetragonal structure with space group I_{41}/a (88), which is isomorphic to $SrWO_4$, and the peaks are accurately indexed. The produced phosphors are observed to form in a single phase, as no additional peaks are evident in the X-ray diffraction pattern. This confirmation suggests the successful occupation of the Y^{3+} site by Sm^{3+} ions. Notably, a shift of the XRD peak at 27.9° to lower angles is observed with increasing Sm^{3+} concentrations, As show in Fig. 1b. This shift can be explained by the substitution of Y^{3+} ions by Sm^{3+} ions and the difference in their ionic radii, leading to an increase in lattice parameters and cell volumes.

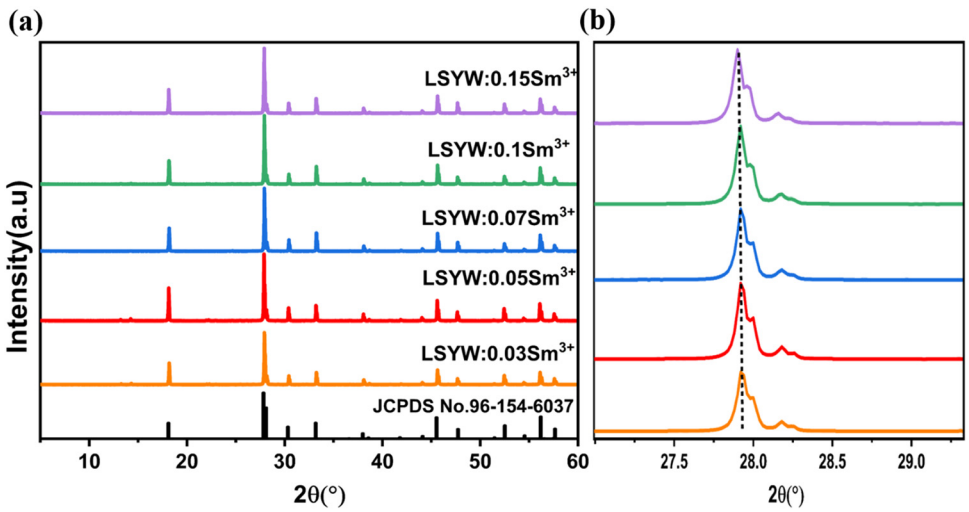

Fig. 1 XRD patterns of the obtained products LSYW:$x$$Sm^{3+}$ (x = 0.03, 0.05, 0.07, 0.1, 0.15).

The SEM pictures of the LSYW:0.05Sm^{3+} phosphors are displayed in Fig. 2. The micrographs that were gathered show that the particles were aggregated and that their sizes fell within 1 μm, it is significant to keep in mind that solid-state chemical processes frequently exhibit this aggregation phenomena.

4. Optical characterization

4.1. UV-visible spectra

Diffuse reflectance spectra are collected over the wavelength range 200–1100 nm as seen in Fig. 3. In order to find the optical band gaps for the powder samples.

According to previously reported literatures,[28,29] we can see that the energy band gap (E_g) and absorption coefficient (α) are related in the way shown below (eqn (1)):

$$(\alpha h\nu)^n = A(h\nu - E_g) \quad (1)$$

where $h\nu$ denotes the energy, A presents constant and the values of m can be 1/2, 2, 3/2 and 3, respectively, when the semiconductor belongs to the allowed direct, allowed indirect, forbidden direct, and forbidden indirect electronic transitions. For LSYW, which is a direct semiconductor, the m number is 1/2.

The E_g values are calculated by plotting $(\alpha h\nu)^2$ against the photon energy $h\alpha$ (eV), as illustrated in Fig. 4. when the absorption coefficient (α) is projected to zero, the band gaps of the LSYW:$x$$Sm^{3+}$ samples decrease with an increase of the "x" value and vary between 3.31 and 3.19 eV.

4.2. PL and PLE characterizations

The excitation (PLE) and emission (PL) spectra of Sm^{3+}-activated LSYW phosphors are shown in Fig. 5. In PLE spectra, a broad charge transfer band from 220 to 350 nm and a number of sharp peaks are observed in the 360–550 nm range. The broad charge transfer band (CTB) was assigned to the $O^{2-} \rightarrow W^{6+}$ transition. The sharp peaks are assigned to the 4f–4f electronic transition of Sm^{3+} ions. Which are located at 345, 362, 377, 405, 418, 439, and 462 nm, corresponding to the transitions $^6H_{5/2} \rightarrow {}^4H_{13/2}$, $^6H_{5/2} \rightarrow {}^4D_{3/2}$, $^6H_{5/2} \rightarrow {}^6P_{7/2}$, $^6H_{5/2} \rightarrow {}^4F_{5/2}$ $^6H_{5/2} \rightarrow {}^6P_{5/2}$, $^6H_{5/2} \rightarrow {}^6G_{9/2}$ and $^6H_{5/2} \rightarrow {}^4I_{(9/2,\,11/2,\,13/2)}$, respectively.[12,30] Since the absorption peak at 405 nm is more intense than the other absorption peaks, the Near UV LED chip can effectively excite the synthesized phosphor,

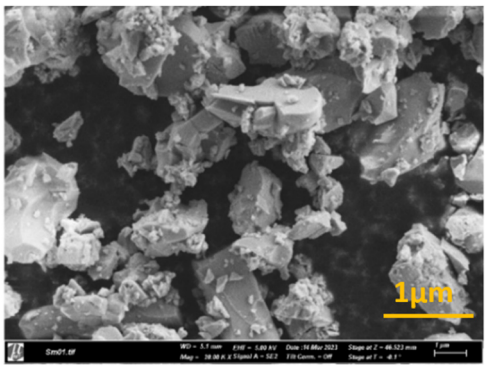

Fig. 2 Scanning electron microscopy images of LSYW doped 0.05Sm^{3+}.

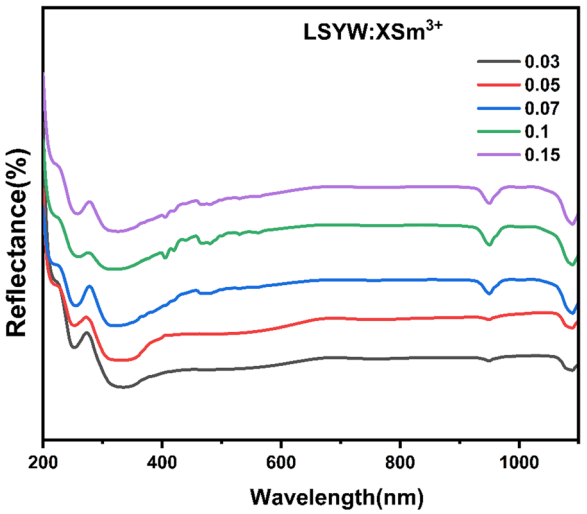

Fig. 3 Diffuse reflectance spectra of LSYW:$x$$Sm^{3+}$($x$ = 0.03, 0.05, 0.07, 0.1 and 0.15).

which is essential for the commercial use of WLEDs. PL emission spectra measured at 405 nm excitation, reveals a variety of peaks in the 550–725 nm wavelength region. A total of five emission bands exists: the band emitted by the $^4F_{3/2} \rightarrow {}^6H_{5/2}$ transition at 523–543, which is weak at room temperature, and the bands emitted by $^6H_{(5/2,\,7/2,\,9/2,\,11/2)}$ transitions whose wavelength ranges are 543–581 nm, 581–634 nm, 634–685 nm, and 685–735 nm, respectively. The Commission International de l'Eclairage (CIE) 1931 chromaticity diagram of the LSYW doped Sm^{3+} at 405 nm is shown in the inset of Fig. 5. The obtained color coordinates are x = 0.60, y = 0.39, and are located in the reddish-orange area of the spectrum.

In order to interpret the energy transfer mechanism, the critical distance (R_c) between two adjacent Sm^{3+} ions in the lattice must be calculated using the Blasse equation (eqn (2)):[31]

$$R_c = 2\left(\frac{3V}{4\pi N X_c}\right)^{1/3} \quad (2)$$

V is the volume of the unit cell, R_c is the critical distance, X_c is the critical concentration, and N is the number of vacant cationic sites in the unit cell that can be occupied by activators.[32] For Sm^{3+}, the open cationic sites are N = 4, and V is taken to be 326.3 cm^{-3}, X_c = 0.05 (as shown in Fig. 6(a) and (b)). A concentration at which the internal decay rate (radiative rate) equals the nonradiative transfer rate is called a concentration quenching concentration.[33] The critical distance of our current system is $R_c \sim 14.6$ Å declares that the exchange interaction has been canceled out ($R_c > 5$ Å), As a result, the only viable approach for non-radiative energy transfer is multipolar interaction. Using Van Uitert's theory, we can explain the concentration quenching. The relationship between luminous intensity and doping concentration is described by the following equation (eqn (3))[34,35]

$$\frac{I}{C} = k\left(1 + \frac{\beta(C)\theta}{3}\right)^{-1} \quad (3)$$

The activator concentration denotes the multipolar interaction constant equal to 6, 8, or 10, which, respectively, correspond to

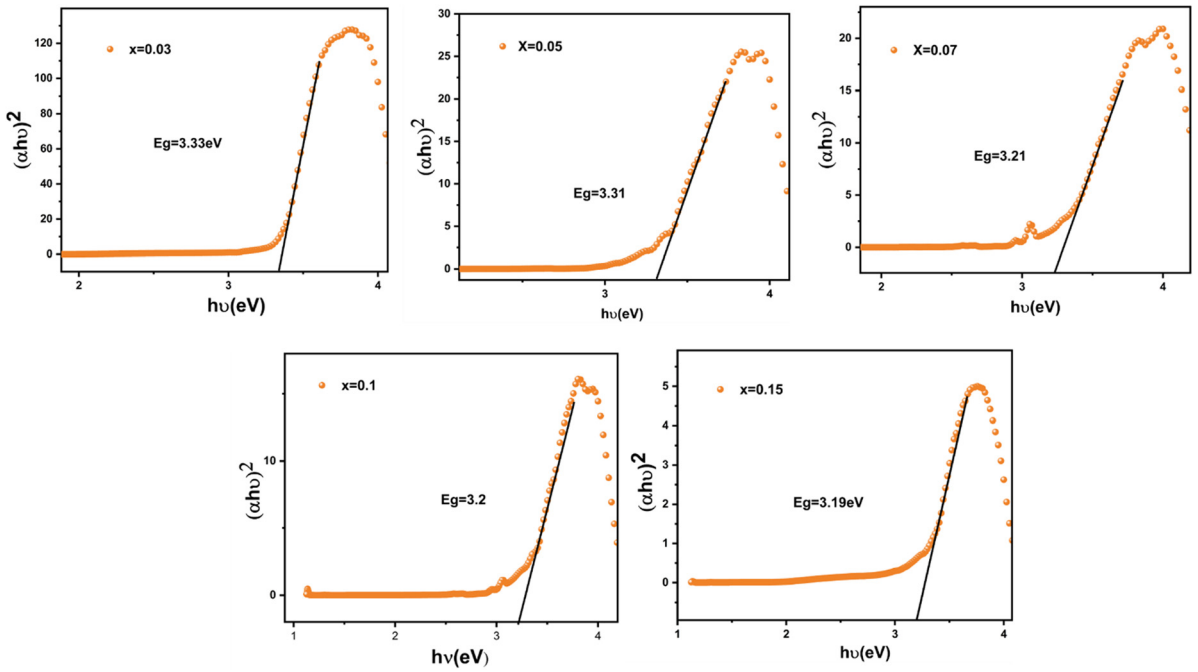

Fig. 4 Plot of $[\alpha h\nu]^2$ *versus* $(h\nu)$ of LSYW doped with x = 0.03, 0.05, 0.07, 0.1 and 0.15Sm^{3+}.

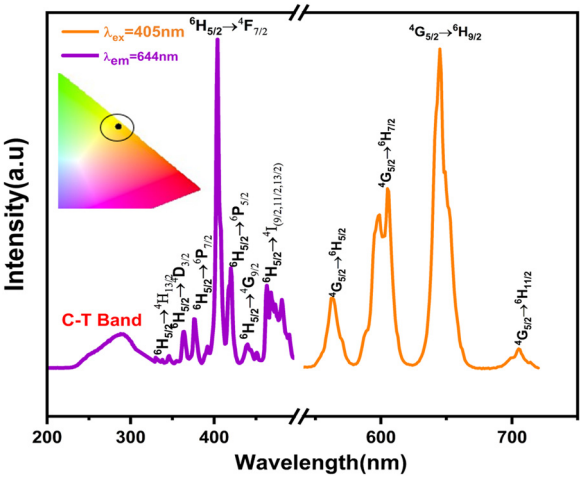

Fig. 5 PLE and PL spectra of the LSYW:5%Sm^{3+} phosphor (inset CIE of the phosphor under 405 nm).

dipole–dipole(d–d), dipole-quadrupole(d–q), and quadrupole-quadrupole(q–q) interactions. Equivalence to Eqn (4) might also be written as:

$$\log\left(\frac{I}{C}\right) = -\left(\frac{\theta}{3}\right)\log(C) + A \qquad (4)$$

wherein A is a constant value.

Fig. 6(c) shows the linear relationship between the log C and log(I/C) values of the LSYW doped $x$$Sm^{3+}$ (x = 0.03, 0.05,0.10 and 0.15) phosphors. The slope $(-\theta/3)$ was determined using linear fitting to be −1.03, (*i.e.*, θ = 3). It is made clear by the estimated slope value and its value that energy is being transferred between the Sm^{3+} ions in the LSYW phosphors. LSYW doped with 0.05Sm^{3+} was used for investigating the optical temperature sensing properties. Fig. 6d illustrates the down-conversion luminescence mechanism of Sm^{3+} ions.[36–39] By absorbing photon energy at 405 nm (24 691 cm^{-1}), Sm^{3+} ions in the $^6H_{5/2}$ level (ground state) are excited to the $^6P_{5/2}$ level (excited state). The Sm^{3+} ions in the excited state continuously proceed *via* NR processes to the $^4F_{3/2}$ level. The population of $^4G_{5/2}$ level increases when the majority of Sm^{3+} ions at $^4F_{3/2}$ level non-radiatively relax to $^4G_{5/2}$ level. Though the radiative transition process, the Sm^{3+} ions at the $^4F_{3/2}$ and $^4G_{5/2}$ levels relax to the $^6H_{5/2}$ level, producing two emission bands with peak wavelengths at 531 nm (~18 832 cm^{-1}) and 568 nm (~17 605 cm^{-1}), respectively. Additionally, the Sm^{3+} ions in the $^4G_{5/2}$ level have the ability to relax to the $^6H_{7/2,9/2,11/2}$ levels, emitting bands of light that are orange-red in color with peak wavelengths of 616 nm (~16 234 cm^{-1}), 651 nm (~15 361 cm^{-1}), and 710 nm (~14 084 cm^{-1}), respectively. Regarding nearby Sm^{3+} ions, there could be four additional cross-relaxation processes as shown in the diagram below.

5. Temperature sensing behavior

For the objective of digging out the optical thermometry features of the manufactured products, the typical temperature-dependent emission spectra of the examined samples with the optimal dopant concentration were determined. Fig. 7a displays down-conversion luminescence for LSYW:0.05Sm^{3+} measured under laser excitation 405 nm at 303–588 K temperature range. The integrated intensities of various emission bands are represented by I_F, I_{G1}, I_{G2}, I_{G2-1}, I_{G2-2}, I_{G3} and I_{G4} to assist the research of the optical temperature sensing properties because

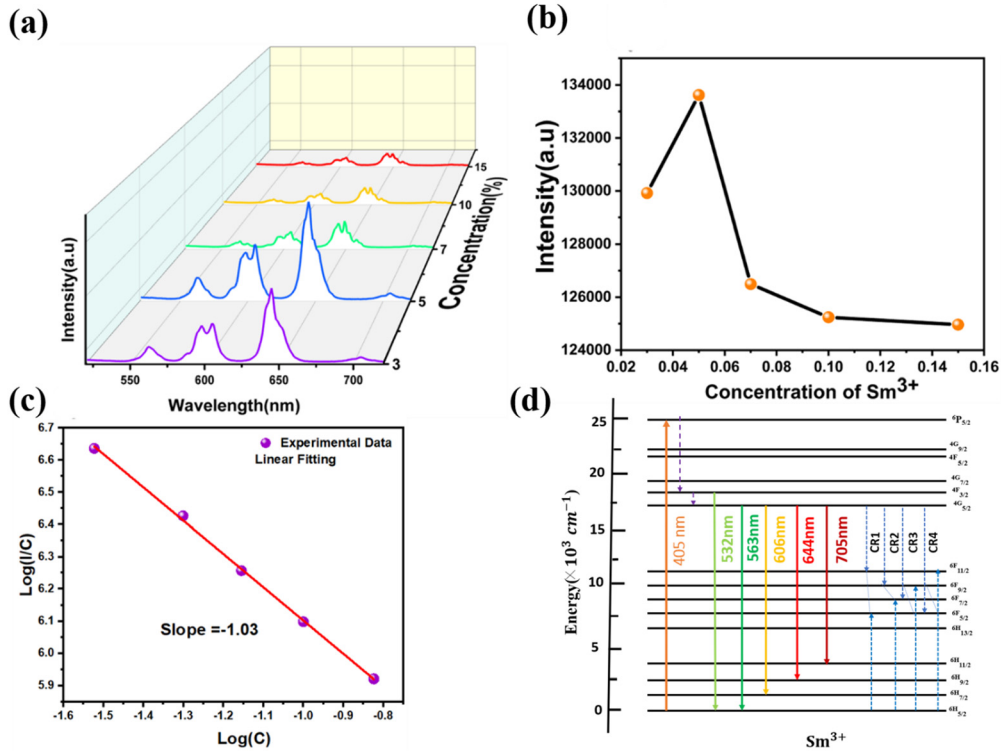

Fig. 6 (a) PL spectra of the LSYW:*x*%Sm^{3+} phosphors, (b) plot of the intensity *vs.* Sm^{3+} concentration (c) linear fitting of log(*I*/*C*) in terms of log(*C*). (d) The mechanism of the down conversion-based luminescence process in Sm^{3+} ions.

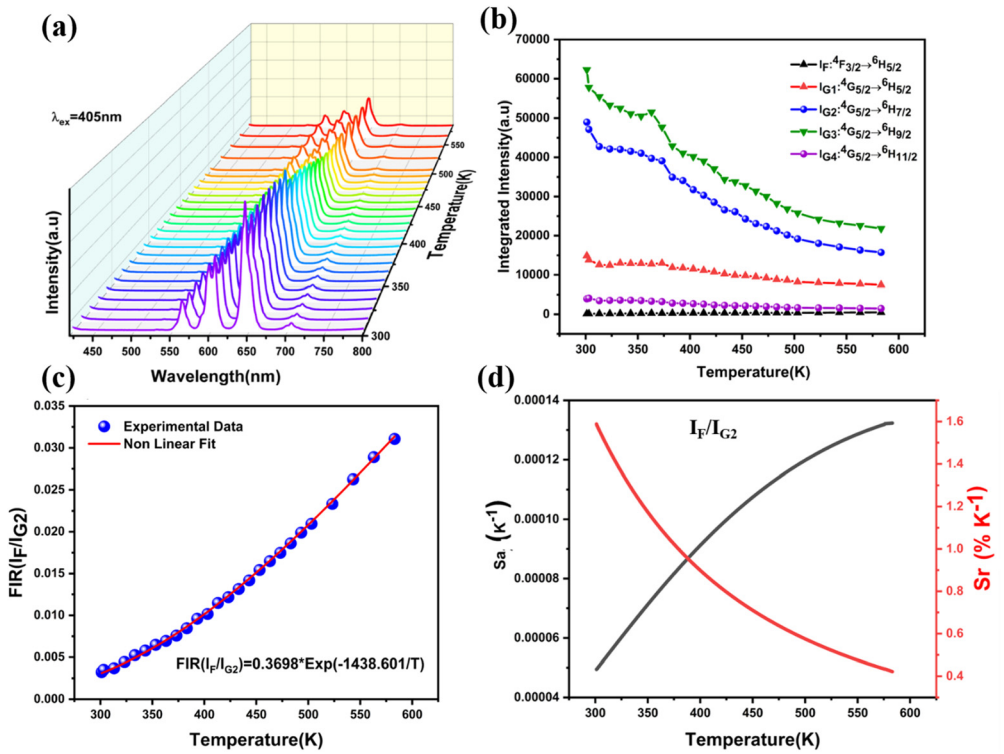

Fig. 7 (a) Down-conversion luminescence spectra of LSYW:0.05Sm^{3+} from 303 to 588 K, (b) the integrated intensities of various emission bands in 303–588 K. (c) The FIR (I_F/I_{G2}) of LSYW:5%Sm^{3+} as function of temperature (303–588 K). (d) The absolute sensitivity and relative sensitivity of I_F/I_{G2}.

the luminescence spectra of LSYW:0.05Sm^{3+} contain several emissions peaks.

The integrated intensities of the $^4F_{3/2} \rightarrow {}^6H_{5/2}$ transition are represented by the band I_F, whereas those of the $^4G_{5/2} \rightarrow {}^6H_{(5/2,\,7/2,\,9/2,\,\text{and}\,11/2)}$ transitions are represented by I_{G1}, I_{G2}, I_{G3}, and I_{G4}, respectively as shown in Fig. 7b. The integrated intensities of two emission sub-bands from the $^4G_{5/2} \rightarrow {}^6H_{7/2}$ transition, with peak wavelengths of 598 nm and 607 nm, respectively, are represented by I_{G2-1} and I_{G2-2} at 303–588 K temperature range. As illustrated in Fig. 7b, the intensity of the fluorescence of the $^4F_{3/2} \rightarrow {}^6H_{5/2}$ transition is weak at low temperature; nevertheless, there is a monotonic increase in intensity as the temperature increases. Because of the thermal quenching effect, fluorescence intensities of the transitions $^4G_{5/2} \rightarrow {}^6H_{(5/2,\,7/2,\,9/2,\,11/2)}$ decrease as temperature increases.

The temperature dependence of FIR of I_F/I_{G2} could be expressed by the Boltzmann's distribution rule as follows (eqn (5)):[40]

$$\mathrm{FIR} = A \times \exp\left(-\frac{\Delta E}{k_B T}\right) \tag{5}$$

where the variables A is a constant, ΔE represents the energy gap between different energy levels, k_B is Boltzmann constant and T is the absolute temperature. The FIR as function of temperature of I_F/I_{G2} is demonstrated in Fig. 7c. The experimental values indicated in the figure was generally in agreement with the fitting curves. I_F/I_{G2} increase monotonically with the temperature, suggesting that the optical detection of temperature can be performed by measuring fluorescence intensity ratio.

The rate at which the FIR changes in response to changes in temperature is known as the absolute sensitivity (S_a). Consequently, the S_a can be written as (eqn (6)).[41–43]

$$S_a = \frac{\mathrm{d(FIR)}}{\mathrm{d}T} = A \cdot \frac{\Delta E}{k_B T^2} \exp\left(-\frac{\Delta E}{k_B T}\right) \tag{6}$$

For the purpose of comparing the sensitivities of various materials, the following relation has been used to calculate relative sensitivity (eqn (7)).[44,45]

$$S_r = \frac{1}{\mathrm{FIR}} \cdot \frac{\mathrm{d(FIR)}}{\mathrm{d}T} = \frac{\Delta E}{k_B T^2} \tag{7}$$

Fig. 7d illustrates the S_a and S_r of I_F/I_{G2} as a function of temperature using eqn (6) and eqn (7), respectively. The curves shown in this figure show that S_a and S_r grow monotonically from 303 K and then decline monotonically after reaching their maximum values. The optical temperature sensor characteristics linked to I_F/I_{G2} is detailed in Table 1. As illustrated in Table 1, LSYW:0.05Sm^{3+} exhibits a lower maximum absolute sensitivity compared to other materials. However, it demonstrates higher maximum relative sensitivities. Furthermore, temperature resolutions (δT) were estimated using eqn (8), where δFIR/FIR represents the uncertainty in the FIR measurement.[46,47]

$$\delta T = \frac{1}{S_r} \cdot \frac{\delta \mathrm{FIR}}{\mathrm{FIR}} \tag{8}$$

where FIR is the thermometric parameter's limit of resolution, that is, the smallest ratio changes that can be observed experimentally. The resolution limit is related to the performance of the thermometer, but it is also controlled by the experimental set up.[48] As a result, enhancing acquisition methods and measurement performance, such as extending integration time and using the average of subsequent measurements to decrease experimental noise, may be one option for increasing the resolution limit. To figure out the limit of detection, 15 measurements were taken at room temperature under similar conditions for Sm^{3+} doped LSYW, and the outcomes are shown in the histograms in Fig. 8a. and the limit of detection (LIR) was determined as the statistical distribution's standard deviation for each method, with values of 0.159 for the I_F/I_{G2}. Fig. 8b display the temperature resolution values δT obtained for I_F/I_{G2} using Eqn (8). It's significant that all of the δT values are less than 1 K at room temperature, which is extremely useful for a wide range of thermometric applications. Therefore, these results obtained using the ratio of emission indicate the decent potential of the LSYW:0.05Sm^{3+} phosphor for temperature sensing applications.

The Commission International de l'Eclairage (CIE) coordinates of phosphors (303–583 K) were obtained in order to more clearly see the change in luminescence color in the phosphors. Fig. 9 shows the sample's CIE chromaticity points at different temperature values. From 203 K to 583 K, there is a change in the colour coordinate from $x = 0.45$, $y = 0.36$ to $x = 0.39$, $y = 0.35$. This phenomenon results from the fact that when temperatures rise, the intensity of the red emission increases. According to these findings, Sm^{3+} doped $LiSrYW_3O_{12}$ phosphor may be a good option to replace the orange component in an orange light-emitting diode.

Table 1 Thermal sensitivities S_a and S_r of optical inorganic temperature sensors single doped with Sm^{3+} ion

Materials	Ratio	Temperature range (K)	$S_{a\,max}$ (K^{-1})	$S_{r\,max}$ (%K^{-1})	Ref.
$YNbO_4$:Sm^{3+}	$^4F_{3/2}$, $^4G_{5/2} \rightarrow {}^6H_{5/2}$	303–773	—	0.43 (500 K)	49
Lu_2O_3:Sm^{3+}	$^4G_{5/2} \rightarrow {}^6H_{5/2}$, $^6H_{9/2}$	293–873	—	0.36 (580 K)	50
Ca_2LaNbO_6:0.05Sm^{3+}	$^4G_{5/2} \rightarrow ({}^6H_{5/2}, {}^6H_{7/2})$	313–573	—	0.23 (353 K)	51
	$^4G_{5/2} \rightarrow ({}^6H_{5/2}, {}^6H_{9/2})$		—	0.22 (313 K)	
$GdVO_4$:Sm^{3+}	$^4F_{3/2}/{}^4G_{5/2} \rightarrow {}^6H_{5/2}$ (I_F/I_{G1})	293–823	4.5×10^{-4} (750 K)	—	52
TZPN:0.5Sm^{3+}	$^4G_{5/2} \rightarrow {}^6H_{5/2}/{}^4G_{5/2} \rightarrow {}^6H_{7/2}$	300–725	—	0.31 (700 K)	53
YVO_4:Sm^{3+}	—	299–466	—	0.36 (466 K)	54
YAG:Sm^{3+}	I_F/I_{G1}	303–1178	3.046×10^{-4} (1129 K)	0.5033 (500 K)	55
YAG:Sm^{3+}	I_{G2-1}/I_{G2-2}	303–1028	5.017×10^{-4} (300 K)	0.1567 (303 K)	55
LSYW:0.05Sm^{3+}	I_F/I_{G2}	301–583	1.32×10^{-5} (583 K)	1.58 (301 K)	This work

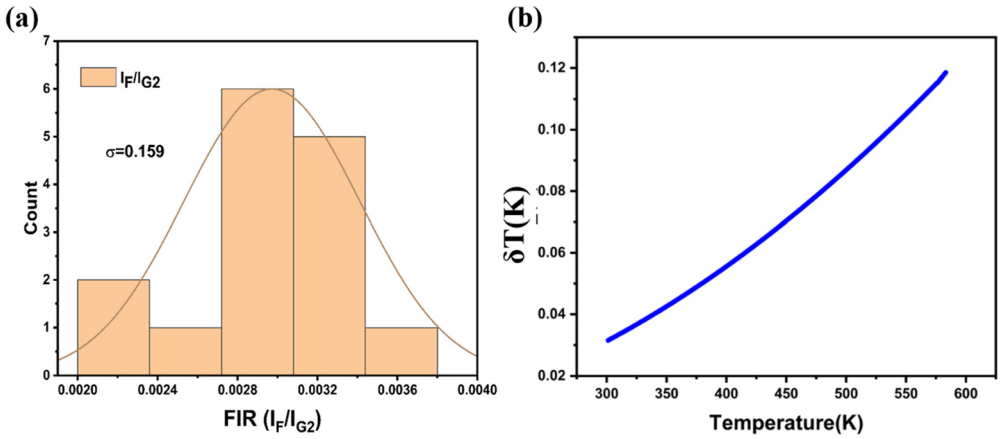

Fig. 8 (a) Standard deviations at RT for FIR (I_F/I_{G2}) obtained using 15 measurements at 300 K. (b) Temperature resolution values δT obtained for I_F/I_{G2}.

6. Conclusions

$LiSrYW_3O_{12}$ (LSYW):$x$$Sm^{3+}$ (x = 0.03, 0.05, 0.07, 0.1, and 0.15) phosphors were synthesized through a high-temperature solid-state reaction, yielding samples with a tetragonal crystal structure, as validated by X-ray diffraction (XRD) analysis. The band gaps of the LSYW:$x$$Sm^{3+}$ samples decrease with increasing Sm^{3+} doping concentrations, ranging from 3.31 to 3.19 eV. Analysis based on the enhanced Van Uitert model and Dexter's theory revealed that D–D interactions primarily contribute to the concentration-dependent luminescence quenching of Sm^{3+} ions, particularly for doping concentrations exceeding 5%. Exploration of the optical temperature sensing properties within the range of 301–583 K revealed notable trends: the fluorescence intensity of the $^4F_{3/2} \rightarrow {}^6H_{5/2}$ transition exhibited a significant increase with rising temperature, while the fluorescence intensities of the $^4G_{5/2} \rightarrow {}^6H_{7/2}$ transition gradually diminished. Maximum sensitivity ratio values (S_r) were determined to be 1.58% K^{-1} (301 K) for $^4F_{3/2} \rightarrow {}^6H_{5/2}/{}^4G_{5/2} \rightarrow {}^6H_{7/2}$ (I_F/I_{G2}). The precision of luminescence thermometry is highlighted by the calculated temperature uncertainty (δT) of less than 1 K, with a minimum at 0.03 K for the I_F/I_{G2} ratio corresponding to the $^4F_{3/2} \rightarrow {}^6H_{5/2}/{}^4G_{5/2} \rightarrow {}^6H_{7/2}$ (I_F/I_{G2}) transitions, underscoring its accuracy and potential as a high-precision optical sensing technique. These findings suggest that Sm^{3+} ions hold promise as optically active centers for luminescence thermometry applications, particularly employing FIR techniques. These results pave the way for the development of luminescent thermometric materials capable of delivering precise temperature information across a broad range of conditions, including demanding and complex scenarios.

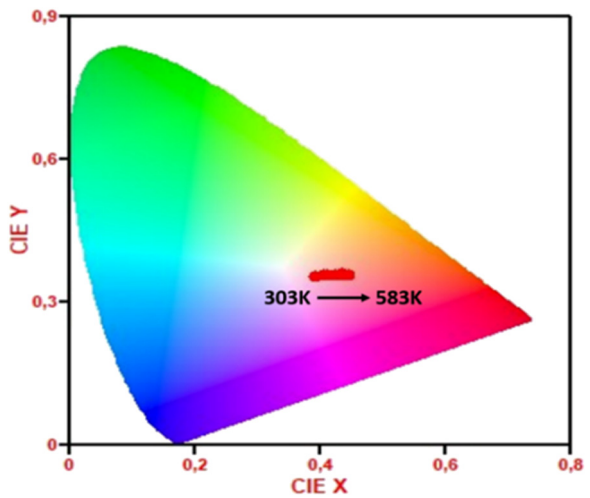

Fig. 9 CIE coordinates changes of LSYW:Sm^{3+} with respect to temperature from 303 to 583 K under 405 nm excitation.

Conflicts of interest

There are no conflicts to declare.

References

1 M. Pieprz, W. Piotrowski, P. Woźny, M. Runowski and L. Marciniak, *Adv. Opt. Mater.*, 2024, **12**, 2301316.
2 C. Hernández-Álvarez, K. Soler-Carracedo, P. Woźny, I. R. Martín and M. Runowski, *J. Mater. Chem. C*, 2024, **12**, 7707–7714.
3 M. Szymczak, P. Woźny, M. Runowski, M. Pieprz, V. Lavín and L. Marciniak, *Chem. Eng. J.*, 2023, **453**, 139632.
4 K. Saidi, W. Chaabani and M. Dammak, *RSC Adv.*, 2021, **11**, 30926–30936.
5 Z. E. A. A. Taleb, K. Saidi and M. Dammak, *RSC Adv.*, 2024, **14**, 8366–8377.
6 Q. Zhang, J. Wang, M. Zhang, W. Ding and Q. Su, *J. Rare Earths*, 2006, **24**, 392–395.
7 L. Yu, F. Hong, Y. Wang, H. Xu, G. Liu, X. Dong, J. Wang and W. Yu, *J. Lumin.*, 2020, **222**, 117155.
8 E. Cavalli, F. Angiuli, I. Kebaïli, M. Dammak, P. Boutinaud and M. Bettinelli, *J. Lumin.*, 2013, **143**, 562–565.
9 I. Kebaïli and M. Dammak, *J. Lumin.*, 2012, **132**, 2092–2097.
10 J. Sun, X. Zhang, Z. Xia and H. Du, *J. Appl. Phys.*, 2012, **111**, 013101.

11 I. Charak, M. Manhas, A. K. Bedyal, H. C. Swart and V. Kumar, *Inorg. Chem. Commun.*, 2023, **160**, 111885.
12 G. Annadurai, S. M. M. Kennedy and V. Sivakumar, *J. Rare Earths*, 2016, **34**, 576–582.
13 R. Cao, G. Quan, Z. Shi, T. Chen, Z. Luo, G. Zheng and Z. Hu, *J. Phys. Chem. Solids*, 2018, **118**, 109–113.
14 C. Liao, R. Cao, W. Wang, W. Hu, G. Zheng, Z. Luo and P. Liu, *Mater. Res. Bull.*, 2018, **97**, 490–496.
15 G. Fan, Z. Tian, X. Wang, S. Tang and Y. Chen, *J. Mater. Sci.: Mater. Electron.*, 2018, **29**, 17681–17688.
16 K. Saidi, I. Kachou, K. Soler-Carracedo, M. Dammak and I. R. Martín, *ACS Appl. Nano Mater.*, 2023, **6**(19), 17681–17690.
17 J. Fan, H. Zhang, J. Wang, Z. Ling, H. Xia, X. Chen, Y. Yu, Q. Lu and M. Jiang, *J. Phys. Appl. Phys.*, 2006, **39**, 1034–1041.
18 P. A. Loiko, V. I. Dashkevich, S. N. Bagaev, V. A. Orlovich, A. S. Yasukevich, K. V. Yumashev, N. V. Kuleshov, E. B. Dunina, A. A. Kornienko, S. M. Vatnik and A. A. Pavlyuk, *J. Lumin.*, 2014, **153**, 221–226.
19 Z. Liu, Q. Meng, H. Liu, C. Yao, Q. Meng, W. Liu and W. Wang, *Opt. Mater.*, 2013, **36**, 384–389.
20 Y. Yin, Y.-N. Li, S. Liu, Y. Jiang, X.-Y. Liu and P. Zhang, *ACS Omega*, 2024, **9**, 10517–10521.
21 C. S. Lim, *Mater. Res. Bull.*, 2016, **75**, 211–216.
22 C. S. Lim, A. Aleksandrovsky, M. Molokeev, A. Oreshonkov and V. Atuchin, *Phys. Chem. Chem. Phys.*, 2015, **17**, 19278–19287.
23 N. Xue, X. Fan, Z. Wang and M. Wang, *J. Phys. Chem. Solids*, 2008, **69**, 1891–1896.
24 C. Ming, F. Song and L. Yan, *Opt. Commun.*, 2013, **286**, 217–220.
25 L. Li, L. Liu, W. Zi, H. Yu, S. Gan, G. Ji, H. Zou and X. Xu, *J. Lumin.*, 2013, **143**, 14–20.
26 C. S. Lim, V. V. Atuchin, A. S. Aleksandrovsky and M. S. Molokeev, *Mater. Lett.*, 2016, **181**, 38–41.
27 F. Ayachi, K. Saidi, M. Dammak, J. Josep Carvajal and M. Cinta Pujol, *RSC Adv.*, 2024, **14**, 13494–13504.
28 K. Saidi and M. Dammak, *J. Solid State Chem.*, 2021, **300**, 122214.
29 Z. E. A. A. Taleb, K. Saidi, M. Dammak, D. Przybylska and T. Grzyb, *Dalton Trans.*, 2023, **52**, 4954–4963.
30 K. Raju, C. G. Balaji and P. Venugopal Reddy, *J. Magn. Magn. Mater.*, 2014, **354**, 383–387.
31 G. Blasse, *J. Solid State Chem.*, 1986, **62**, 207–211.
32 Y. Tian, Y. Liu, R. Hua, L. Na and B. Chen, *Mater. Res. Bull.*, 2012, **47**, 59–62.
33 G. S. Ofelt, *J. Chem. Phys.*, 2004, **37**, 511–520.
34 Z. Yahiaoui, M. A. Hassairi, M. Dammak and E. Cavalli, *J. Alloys Compd.*, 2018, **763**, 56–61.
35 F. Ayachi, K. Saidi, W. Chaabani and M. Dammak, *J. Lumin.*, 2021, **240**, 118451.
36 W. Ryba-Romanowski, A. Strzęp, R. Lisiecki, M. Berkowski, H. Rodriguez-Rodriguez and I. R. Martin, *Opt. Mater. Express*, 2014, **4**, 739–752.
37 S. Q. Mawlud, M. M. Ameen, Md. R. Sahar, Z. A. S. Mahraz and K. F. Ahmed, *Opt. Mater.*, 2017, **69**, 318–327.
38 A. Mohan Babu, B. C. Jamalaiah, T. Sasikala, S. A. Saleem and L. Rama Moorthy, *J. Alloys Compd.*, 2011, **509**, 4743–4747.
39 S. Karki, C. R. Kesavulu, H. J. Kim, J. Kaewkhao, N. Chanthima and Y. Ruangtaweep, *J. Lumin.*, 2018, **197**, 76–82.
40 K. Saidi, C. Hernández-Álvarez, M. Runowski, M. Dammak and I. R. Martín, *Dalton Trans.*, 2023, **52**, 14904–14916.
41 F. Huang and D. Chen, *J. Mater. Chem. C*, 2017, **5**, 5176–5182.
42 H. Zhou, N. An, K. Zhu, J. Qiu, L. Yue, L.-G. Wang and L. Ye, *J. Lumin.*, 2021, **229**, 117656.
43 Y. Gao, F. Huang, H. Lin, J. Zhou, J. Xu and Y. Wang, *Adv. Funct. Mater.*, 2016, **26**, 3139–3145.
44 F. Ayachi, K. Saidi, M. Dammak, W. Chaabani, I. Mediavilla-Martínez and J. Jiménez, *Mater. Today Chem.*, 2023, **27**, 101352.
45 N. An, L. Ye, R. Bao, L. Yue and L.-G. Wang, *J. Lumin.*, 2019, **215**, 116657.
46 J. Rocha, C. D. S. Brites and L. D. Carlos, *Chem. – Eur. J.*, 2016, **22**, 14782–14795.
47 F. Ayachi, K. Saidi, K. Soler-Carracedo, M. Dammak and I. R. Martín, *J. Alloys Compd.*, 2023, **961**, 171146.
48 J.-C. G. Bunzli and V. K. Pecharsky, *Handbook on the Physics and Chemistry of Rare Earths: Including Actinides*, Elsevier, 2016.
49 L. R. Đačanin, S. R. Lukić-Petrović, D. M. Petrović, M. G. Nikolić and M. D. Dramićanin, *J. Lumin.*, 2014, **151**, 82–87.
50 V. Lojpur, Ž. Antić, R. Krsmanović, M. M. Medić, M. G. Nikolić and M. Dramićanin, *J. Serbian Chem. Soc.*, 2012, **77**, 1735–1746.
51 A. Zhang, Z. Sun, M. Jia, Z. Fu, B. C. Choi, J. H. Jeong and S. H. Park, *J. Alloys Compd.*, 2021, **889**, 161671.
52 M. G. Nikolić, D. J. Jovanović, V. D. Jordjević, Ž. Antić, R. M. Krsmanović and M. D. Dramićanin, *Phys. Scr.*, 2012, 014063.
53 B. Klimesz, R. Lisiecki and W. Ryba-Romanowski, *J. Alloys Compd.*, 2019, **788**, 658–665.
54 I. E. Kolesnikov, E. V. Golyeva, M. A. Kurochkin, E. Y. Kolesnikov and E. Lähderanta, *J. Lumin.*, 2020, **219**, 116946.
55 K. Zhu, H. Zhou, J. Qiu, L.-G. Wang and L. Ye, *J. Alloys Compd.*, 2022, **890**, 161844.